Observational constraints on atmospheric and oceanic cross-equatorial heat transports: revisiting the precipitation asymmetry problem in climate models

www.reading.ac.uk/centaur

CentAUR

Central Archive at the University of Reading

Reading's research outputs online

CrossMark

Observational constraints on atmospheric and oceanic cross-equatorial heat transports: revisiting the precipitation asymmetry problem in climate models

Norman G. Loeb[1] · Hailan Wang[2] · Anning Cheng[2] · Seiji Kato[1] · John T. Fasullo[3] ·
Kuan-Man Xu[1] · Richard P. Allan[4]

Abstract Satellite based top-of-atmosphere (TOA) and surface radiation budget observations are combined with mass corrected vertically integrated atmospheric energy divergence and tendency from reanalysis to infer the regional distribution of the TOA, atmospheric and surface energy budget terms over the globe. Hemispheric contrasts in the energy budget terms are used to determine the radiative and combined sensible and latent heat contributions to the cross-equatorial heat transports in the atmosphere (AHT_{EQ}) and ocean (OHT_{EQ}). The contrast in net atmospheric radiation implies an AHT_{EQ} from the northern hemisphere (NH) to the southern hemisphere (SH) (0.75 PW), while the hemispheric difference in sensible and latent heat implies an AHT_{EQ} in the opposite direction (0.51 PW), resulting in a net NH to SH AHT_{EQ} (0.24 PW). At the surface, the hemispheric contrast in the radiative component (0.95 PW) dominates, implying a 0.44 PW SH to NH OHT_{EQ}. Coupled model intercomparison project phase 5 (CMIP5) models with excessive net downward surface radiation and surface-to-atmosphere sensible and latent heat transport in the SH relative to the NH exhibit anomalous northward AHT_{EQ} and overestimate SH tropical precipitation. The hemispheric bias in net surface radiative flux is due to too much longwave surface radiative cooling in the NH tropics in both clear and all-sky conditions and excessive shortwave surface radiation in the SH subtropics and extratropics due to an underestimation in reflection by clouds.

1 Introduction

A number of recent studies have shown a strong link between hemispheric asymmetry in tropical precipitation and the atmospheric energy budget. The energetics framework has been used to explain why the mean position of the Intertropical Convergence Zone (ITCZ) is in the Northern Hemisphere (Frierson et al. 2013; Marshall et al. 2013), to demonstrate the large-scale circulation and precipitation responses to changes in the hemispheric distribution of heating due to various forcing mechanisms (Yoshimori and Broccoli 2008; Kang et al. 2008, 2009; Frierson and Hwang 2012; Hwang et al. 2013; Voigt et al. 2014; Haywood et al. 2015), and to evaluate the realism of climate models using observations (Hwang and Frierson 2013; Donohoe et al. 2013).

Satellite observations indicate that there is a net gain of radiative energy at the top-of-atmosphere (TOA) in the Southern Hemisphere (SH) and a net loss in the Northern Hemisphere (NH). To compensate, the combined atmospheric and oceanic circulations transport energy across the equator from the SH to the NH (Frierson et al. 2013; Marshall et al. 2013). A common approach for inferring the oceanic contribution to cross-equatorial energy transport is to estimate the hemispheric mean surface energy budget in the SH and NH from the difference between satellite TOA net radiation and divergence of total atmospheric energy

✉ Norman G. Loeb
norman.g.loeb@nasa.gov

1   NASA Langley Research Center, Hampton, VA, USA

2   Science Systems and Applications, Inc., Hampton, VA, USA

3   National Center for Atmospheric Research, Boulder, CO, USA

4   Department of Meteorology, University of Reading, Reading, UK

 Springer

transport from reanalysis (Trenberth and Caron 2001; Trenberth and Fasullo 2008; Frierson et al. 2013; Marshall et al. 2013; Liu et al. 2015). It is found that the asymmetry in the SH and NH surface energy budget is twice that at the TOA, implying a SH to NH ocean heat transport (mainly in the Atlantic meridional overturning circulation) and an atmospheric heat transport in the opposite direction (Fig. 1). Frierson et al. (2013) and Marshall et al. (2013) argue that the latter is accomplished via a southward cross-equatorial energy transport in the upper branch of the Hadley Circulation (mainly dry static energy) and a northward cross-equatorial moisture transport in the lower branch of the Hadley Circulation, resulting in an ITCZ located just north of the equator. Both studies emphasize that the hemispheric asymmetry of atmospheric heating is primarily due to ocean heat transport across the equator and slab ocean aquaplanet simulations were used to illustrate the link between the ITCZ's location north of the equator and cross-equatorial ocean energy transport.

Here, we expand upon these earlier studies by also considering estimates of hemispheric asymmetry in surface and atmospheric radiation budget derived from satellite observations. This enables a decomposition of cross-equatorial heat transport in terms of radiative and non-radiative (i.e., combined latent and sensible heat) components. We demonstrate the utility of this decomposition by comparing the observational results with output from 30 models that participated in the Coupled Model Intercomparison Project Phase 5 (CMIP5) (Taylor et al. 2012). This framework is also used to revisit the precipitation asymmetry problem in climate models exhibiting excessive SH tropical precipitation compared to observations (Hwang and Frierson 2013).

2 Data and methods

2.1 Cross-equatorial heat transport

Previous studies (Trenberth and Fasullo 2008; Fasullo and Trenberth 2008) have shown that the monthly net surface energy flux (F_s) at a given location can be inferred from the vertically integrated atmospheric energy budget equation using satellite observations of net downward TOA radiation (R_T) and reanalysis output of total atmospheric energy tendency $\left(\frac{\partial A_E}{\partial t}\right)$ and divergence ($\nabla \cdot F_A$):

$$F_s = R_T - \nabla \cdot F_A - \frac{\partial A_E}{\partial t} \tag{1}$$

where

$$A_E = \frac{1}{g} \int_0^{p_s} (h + k)dp$$

$$F_A = \frac{1}{g} \int_0^{p_s} (h + k)\vec{u}\,dp$$

A_E is the vertical integral of total energy and F_A is the atmospheric heat transport, g is the acceleration due to gravity, p is pressure, and $\vec{u}$ is horizontal velocity. Total energy is the sum of moist static energy, $h = c_pT + gz + Lq$, and kinetic energy, k, where c_p is the specific heat capacity of air at constant pressure, T is absolute temperature, z is height, L is latent heat of condensation, and q is specific humidity. In Eq. (1), F_s is defined as positive downwards.

Fig. 1 Implied cross-equatorial energy transports in the atmosphere and ocean inferred from hemispheric asymmetries in CERES TOA and surface energy budgets and mass corrected divergence in ERA-interim atmospheric total energy transport
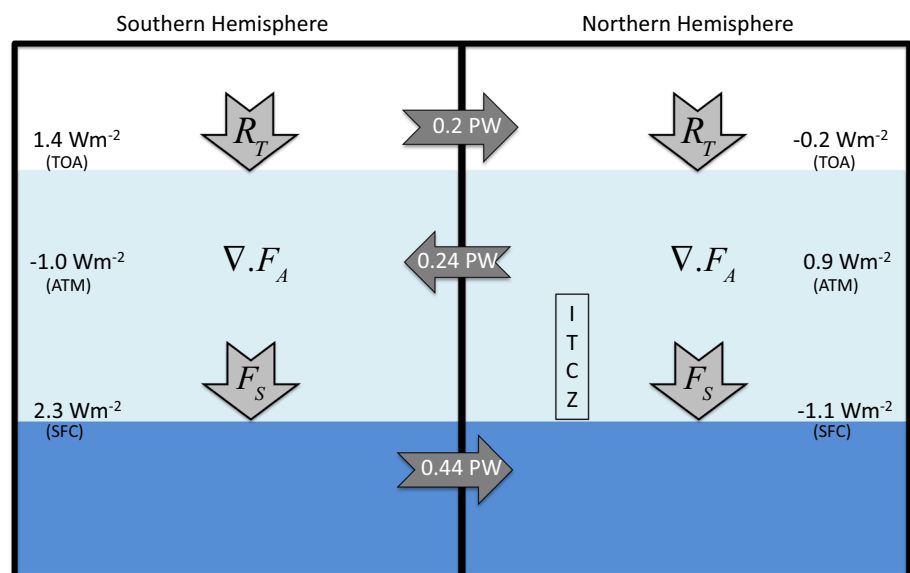
If the net downward radiative flux at the surface (R_s) is known, an estimate of surface sensible and latent heat fluxes, defined as positive downwards, is determined from:

$$Q_S = H_L + H_S = F_S - R_S \tag{2}$$

where H_L is surface latent heat flux and H_S is surface sensible heat flux.

Noting that atmospheric heat transport divergence averaged over the Southern Hemisphere equals the heat transport across the equator, Donohoe et al. (2013) derive an expression for the atmospheric cross-equatorial heat transport (AHT_{EQ}) in terms of the hemispheric contrast in the TOA and surface energy budgets and the total energy tendency:

$$AHT_{EQ} = \frac{1}{2}\left(\Delta R_T - \Delta F_S - \Delta \frac{\partial A_E}{\partial t}\right) \tag{3}$$

where Δ denotes the SH minus NH difference. AHT_{EQ} is converted from W m^{-2} to PW using 1 W m^{-2} = 0.255 PW (assuming a hemispheric surface area of 2.55×10^{14} m^2). A similar expression for ocean equatorial heat transport (OHT_{EQ}) is:

$$OHT_{EQ} = \frac{1}{2}\left(\Delta F_S - \Delta \frac{\partial O_E}{\partial t}\right) \tag{4}$$

where $\frac{\partial O_E}{\partial t}$ is the tendency in ocean heat content.

Equations (3) and (4) can be decomposed into radiative and non-radiative contributions:

$$AHT_{EQ} = \frac{1}{2}\left(\Delta R_A + \Delta Q_A - \Delta \frac{\partial A_E}{\partial t}\right) \tag{5}$$

$$OHT_{EQ} = \frac{1}{2}\left(\Delta R_S + \Delta Q_S - \Delta \frac{\partial O_E}{\partial t}\right) \tag{6}$$

where $R_A = R_T - R_S$ is net atmospheric radiation, and $Q_A = -Q_S$ is combined surface sensible and latent heat flux transfer from the surface to the atmosphere. In Eqs. (5) and (6), the contribution from the hemispheric difference in atmospheric and oceanic tendencies ($\Delta \frac{\partial A_E}{\partial t}$ and $\Delta \frac{\partial O_E}{\partial t}$, respectively) can be neglected, as these are at least an order-of-magnitude smaller than hemispheric differences in the other terms (Loeb et al. 2014; Durack et al. 2014; Drijfhout et al. 2014; Roemmich et al. 2015).

2.2 Data

2.2.1 Observations

Radiative fluxes are from the Clouds and the Earth's Radiant Energy System (CERES) Energy Balanced and Filled (EBAF) Ed2.8 product for the TOA (Loeb et al. 2009, 2012) and surface (Kato et al. 2013). We consider a 12-year climatology from January 2001 to December 2012.

CERES broadband radiation instruments aboard the *Terra* (launched in December 1999) and *Aqua* (launched in May 2002) satellites are used along with 3-hourly geostationary satellite observations that have been cross-calibrated with the more accurate Moderate Resolution Imaging Spectroradiometer (MODIS) imager (Salomonson et al. 1989), which is also aboard *Terra* and *Aqua*. The methodology used to enhance CERES *Terra* and *Aqua* diurnal sampling with geostationary data is described in detail in Doelling et al. (2013). Computed surface radiative fluxes in EBAF are generated using a two-step process (Kato et al. 2013). The first step is to compare computed TOA radiative fluxes from the CERES SYN1 deg Ed3A product (Rutan et al. 2015) with observed CERES EBAF Ed2.8 TOA fluxes. The SYN1 deg computed fluxes are based upon radiative transfer model calculations using MODIS and geostationary satellite-retrieved surface, cloud, and aerosol properties, and reanalysis data for atmospheric state. Next, a Lagrange multiplier procedure is used to objectively adjust the inputs to the radiative transfer model calculation within their uncertainties to ensure consistency between computed TOA fluxes and observed CERES EBAF TOA fluxes. The adjusted input parameters are then used to determine EBAF surface radiative fluxes that are internally consistent with EBAF TOA fluxes. Input parameter uncertainties are determined through comparisons with observations from the Atmospheric Infrared Sounder (AIRS; Chahine et al. 2006), Cloud–Aerosol Lidar and Infrared Pathfinder Satellite Observations (CALIPSO; Winker et al. 2010) and CloudSat (Stephens et al. 2008) (see Kato et al. 2013 for details).

Total atmospheric energy divergence ($\nabla \cdot F_A$) for January 2001–December 2012 is obtained from NCAR (2014), which provides mass corrected vertically integrated energy budget terms (Trenberth et al. 2011) for European Center for Medium-Range Weather Forecasts (ECMWF) Interim Re-Analysis (ERA-Interim; Dee et al. 2011) data. F_s is determined as a residual from the terms on the right-hand side of Eq. (1), and $Q_A = -Q_S$, which is determined from the expression on the right-hand side of Eq. (2).

Monthly precipitation rates from the Global Precipitation Climatology Project (GPCP; Adler et al. 2003; Huffman et al. 2009) version 2.2 are also used in this study. Over ocean, GPCP combines precipitation information from the Special Sensor Microwave Imager (SSM/I) aboard the Defense Meteorological Satellite, infrared precipitation estimates from geostationary satellites, the Atmospheric Infrared Sounder (AIRS) data from the NASA Aqua, the Television Infrared Observation Satellite Program (TIROS) Operational Vertical Sounder (TOVS) and Outgoing Longwave Radiation Precipitation Index (OPI) data from the NOAA satellites. Over land, it relies on gauge data to calibrate the microwave and infrared-based satellite estimates.

Because cross-equatorial heat transport is inferred from hemispheric differences in energy budget terms, any systematic bias common to both hemispheres cancels in the difference. As a result, the observational uncertainty is smaller than that of a global or hemispheric mean value. As described in detail in "Appendix", we estimate the uncertainty in total cross-equatorial heat transport (HT_{EQ}) to be 0.05 PW. For AHT_{EQ} and OHT_{EQ}, uncertainties are 0.04 PW and 0.07 PW, respectively. Uncertainties for individual components are 0.10 PW, 0.12 PW and 0.11 PW for ΔR_S, ΔQ_S and ΔR_A, respectively.

2.2.2 CMIP5 model simulations

Multiple coupled atmosphere–ocean model simulations from the CMIP5 historical experiment, which applies realistic changes in radiative forcings since 1850, are considered for the 1980–2004 period. In contrast to the observational approach, where F_S and Q_S are determined as residuals and $\nabla \cdot F_A$ is computed directly, F_S and Q_S are obtained directly from CMIP5 standard model output of surface energy budget terms (R_S, H_L, and H_S) and $\nabla \cdot F_A$ is determined as a residual term in Eq. (1). Combining the CMIP5 surface energy budget terms with model output of R_T provides the radiative and combined latent and sensible heat flux contributions to AHT_{EQ} and OHT_{EQ} (Eqs. 5 and 6). Originally, a total of 38 CMIP5 models were considered (Table 1). However, many models were found to have large inconsistencies between their global mean net TOA and surface energy budgets, implying the existence of a spurious nonzero total atmospheric energy divergence. Here we only consider CMIP5 models in which the multiyear globally averaged difference $R_T - F_S$ (or equivalently $\nabla \cdot F_A$) is smaller than 1 W m^{-2}; only 30 satisfy this criterion (Table 1).

It is worth noting that while CMIP5 latent heat flux accounts for evaporation and sublimation, it does not consider the loss of surface energy associated with snowfall over ice-free ocean that melts on contact with the surface. To include this contribution, we subtract the following expression over open ocean from H_L inferred from each CMIP5 model:

$$H_L^f = L_f \rho_l S_R \tag{7}$$

where L_f is the latent heat of fusion of water (334 kJ kg^{-1}), ρ_l is the density of water (1000 kg m^{-3}), and S_R is the water-equivalent snowfall rate. For S_R in mm day^{-1}, this corresponds to 3.866 S_R W m^{-2}. We assume a distribution of ice-free ocean from the observed HadISST climatological (1980–2004) sea–ice fraction for all models. Any error introduced by using the HadISST sea ice fraction instead of those from the individual CMIP5 models is expected to

be small. Globally, the latent heat of snow fusion over open ocean is between 0.1 and 0.5 W m^{-2}. While this is small compared to latent heat flux by evaporation and sublimation, it is of the same magnitude as the globally averaged value of R_T, and therefore is an important term when applying the above energy budget criterion for model selection.

3 Results

3.1 Regional and zonal mean atmospheric energy budget

We first compare observed and CMIP5 multi-model climatological mean regional distributions of the radiative and combined latent and sensible heat flux terms in the atmospheric energy budget (Fig. 2a–i). The multi-model mean is determined by averaging fluxes from CMIP5 models 1–30 in Table 1 after interpolating each model's output to a common grid of 1° latitude by 1° longitude, which is the spatial resolution of the CERES EBAF data. The observations fall within the model interquartile range in 26, 35 and 38 % of the regions for R_A, Q_A, and $\nabla \cdot F_A$, respectively. For in R_A, these typically occur for regions having an absolute model-observed difference <5W m^{-2} (80 % of the cases), whereas for Q_A and $\nabla \cdot F_A$, a similar percentage is realized for regions with an absolute difference <10 W m^{-2}.

Regional patterns in R_A are similar between observations and models (Fig. 2a, b), although marked differences are apparent in marine stratocumulus regions off the west coasts of North and South America where the models underestimate atmospheric radiative cooling (Fig. 2c). The likely reasons include an underestimation of non-overlapped low cloud in CMIP5 models (Nam et al. 2012) and a dry bias in the marine boundary layer (John and Soden 2007). The models also show less cooling in middle and high latitudes in both hemispheres. Conversely, CMIP5 atmospheric radiative cooling is more pronounced in convective regions such as central Africa, the Pacific Warm Pool, ITCZ, and the Amazon. Consistent with these results, Li et al. (2013) found that CMIP5 models underestimate TOA reflected solar and overestimate outgoing longwave radiation in convectively active regions of the tropics due to an underestimation in the amount of total ice and liquid atmospheric water content.

Both the observations and models show larger combined latent and sensible heat fluxes over the subtropical oceans compared to other latitudes (Fig. 2d, e), with a maximum at about 20°S in the southern Indian Ocean. Intense heat flux gain also occurs in the warm western boundary currents, such as the Gulf Stream off the east coast of the United States, the Kuroshio Current near Japan, the Agulhas Current off the coast of South Africa, the Brazilian

Table 1 List of CMIP5 models considered in this study

Model number	Model name	Country/model group	Resolution (Lon × Lat)	Rt-Fs
1	ACCESS1.0	Australia/ACCESS	1.875° × 1.25°	−0.38
2	ACCESS1.3		1.875° × 1.25°	−0.65
3	CCSM4	US/NCAR	1.25° × 0.9375°	−0.35
4	CESM1-BGC		1.25° × 0.9375°	−0.34
5	CESM1-FASTCHEM		1.25° × 0.9375°	−0.35
6	CESM1-WACCM		2.5° × 1.89°	−0.24
7	CSIRO-Mk3.6.0	Australia/CSIRO	1.875° × 1.86°	0.33
8	CanESM2	Canada	2.8125° × 2.79°	0.19
9	GFDL-CM3	US/GFDL	2.5° × 2.0°	−0.36
10	GFDL-ESM2G		2.5° × 2.01°	−0.55
11	GFDL-ESM2 M		2.5° × 2.01°	−0.56
12	GISS-E2-H	US/GISS	2.5° × 2.0°	−0.42
13	GISS-E2-H-CC		2.5° × 2.0°	−0.40
14	GISS-E2-R		2.5° × 2.0°	−0.39
15	GISS-E2-R-CC		2.5° × 2.0°	−0.39
16	HadCM3	UK/Met Office	3.75° × 2.5°	−0.29
17	HadGEM2-CC		1.875° × 1.25°	−0.48
18	HadGEM2-ES		1.875° × 1.25°	−0.46
19	IPSL-CM5A-LR	France/IPSL	3.75° × 1.89°	0.32
20	IPSL-CM5A-MR		2.5° × 1.27°	0.33
21	IPSL-CM5B-LR		3.75° × 1.89°	−0.59
22	MIROC4 h	Japan/MIROC	0.5625° × 0.56°	−0.50
23	MIROC5		1.40625° × 1.40°	0.24
24	MPI-ESM-LR	Germany/MPI	1.875° × 1.86°	0.09
25	MPI-ESM-MR		1.875° × 1.86°	0.21
26	MPI-ESM-P		1.875° × 1.86°	0.12
27	MRI-CGCM3	Japan/MRI	1.125° × 1.12°	−0.19
28	MRI-ESM1		1.125° × 1.12°	−0.20
29	bcc-csm1-1	China/BCC	2.8125° × 2.79°	−0.97
30	bcc-csm1-1-m		1.125° × 1.12°	−0.99
31	*BNU-ESM*	*China/BNU*	*2.8125° × 2.79°*	*1.75*
32	*CNRM-CM5*	*France/CNRM*	*1.40° × 1.40°*	*3.14*
33	*CNRM-CM5.2*		*1.40° × 1.40°*	*3.09*
34	*FGOALS-g2*	*China/IAP*	*2.8125° × 3.05°*	*1.23*
35	*MIROC-ESM*	*Japan/MIROC*	*2.8125° × 2.79°*	*−4.19*
36	*MIROC-ESM-CHEM*		*2.8125° × 2.79°*	*−4.37*
37	*NorESM1-M*	*Norway*	*2.5° × 1.89°*	*1.63*
38	*NorESM1-ME*		*2.5° × 1.89°*	*1.65*

Because models 31–38 (italicized) fail to meet the 1 W m^{-2} consistency criterion between global mean net TOA and surface energy budgets (R_T–F_S), these models were excluded from the analysis

Current off of South America, and the East Australian Current. There is also qualitative agreement in regions with cooler sea surface temperatures, such as the northern Pacific Ocean and Southern Ocean, as well as over vast land masses in the northern hemisphere (e.g., Saharan desert, Asia, North America). The largest differences occur near the equator over the central and eastern Pacific Ocean as well as over the Indian Ocean (Fig. 2f). Differences greater in magnitude than 20 W m^{-2} also occur in the North Pacific Ocean between 30°N and 50°N and over the Indian Ocean between 20°S and 40°S. Regional patterns in $\nabla \cdot F_A$ (Fig. 2g, h) show a divergence of heat transport equatorward of 40° latitude in regions influenced by deeper convective cloud and cirrus anvils such as the Indian ocean, western Pacific, the tropical Atlantic and equatorial Africa and South America. Convergence of energy in the
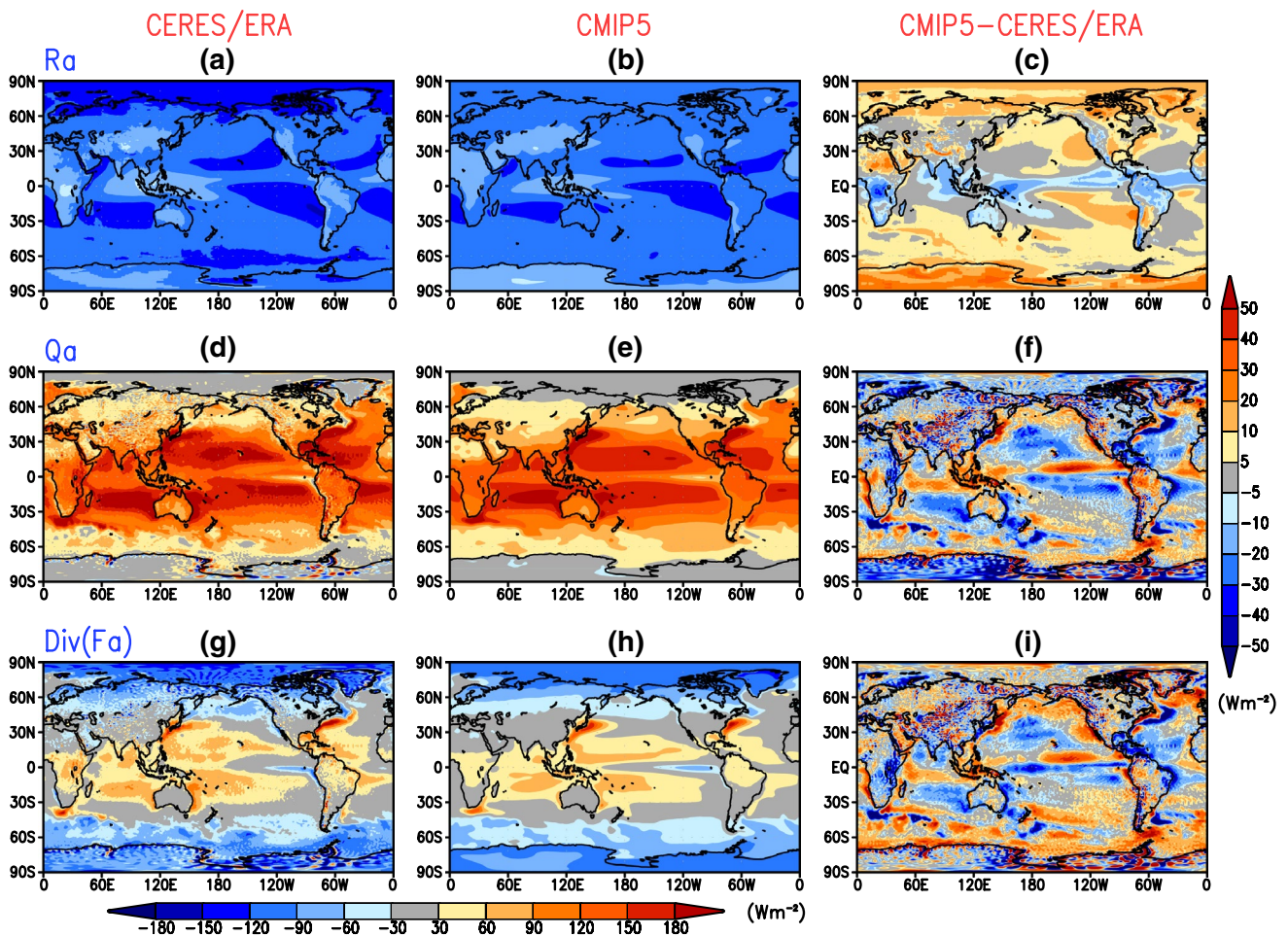
Fig. 2 R_A (**a**, **b**), Q_A (**d**, **e**) and $\nabla \cdot F_A$ (**g**, **h**) inferred from CERES radiative fluxes and mass corrected ERA-interim total atmospheric energy tendency and divergence (*left column*) and from CMIP5 multi-model mean surface and TOA energy budget terms (*middle column*). CMIP5 minus observed **c** R_A, **f** Q_A and **i** $\nabla \cdot F_A$

atmosphere is evident at latitudes greater than 40°, where atmospheric radiative cooling generally dominates over atmospheric heating by latent and sensible heat fluxes. Local maxima in $\nabla \cdot F_A$ are associated with the western boundary currents, while a minimum occurs in the eastern Pacific Ocean cold tongue region.

The atmospheric energy budget terms show remarkable hemispheric symmetry (Fig. 3a–i). Zonal mean hemispheric differences (vertical bars in Fig. 3) are generally less than 20 % of the zonal mean in the tropics and midlatitudes, and closely track one another poleward of 65°. There is a slightly greater contrast in $\nabla \cdot F_A$ between the tropics and midlatitudes in the SH (Fig. 3g), implying a stronger tropical-to-midlatitude heat transport in the SH atmosphere compared to the NH. The stronger convergence of heat in the SH midlatitudes (Fig. 3g) is associated with both increased atmospheric radiative cooling (Fig. 3a) and less latent and sensible heating (Fig. 3d) compared to the NH. Frierson et al. (2013) argue that in response to the weaker poleward heat transport

in the NH lower latitudes, the tropical mean atmospheric circulation transports energy from the NH to the SH via a southward cross-equatorial flow. At the same time, hemispheric symmetry in TOA radiation at midlatitudes (Fig. 2a in Frierson et al. 2013) implies a greater ocean heat transport into the NH midlatitudes. Overall, the CMIP5 multi-model mean results show a similar latitudinal dependence in each hemisphere as the observations (Fig. 3b, e, h). The largest discrepancy occurs in the deep tropics around 5°N, where differences are greater in magnitude than 10 W m^{-2} for Q_A (Fig. 3f) and 5 W m^{-2} for $\nabla \cdot F_A$ (Fig. 3i). These differences are primarily due to excessive Q_A in the ITCZ region of the eastern Pacific Ocean region (Fig. 2f).

3.2 Energy budget hemispheric asymmetry and cross-equatorial heat transport

At the TOA, the remarkable hemispheric symmetry in absorbed shortwave (SW) radiation in the observations
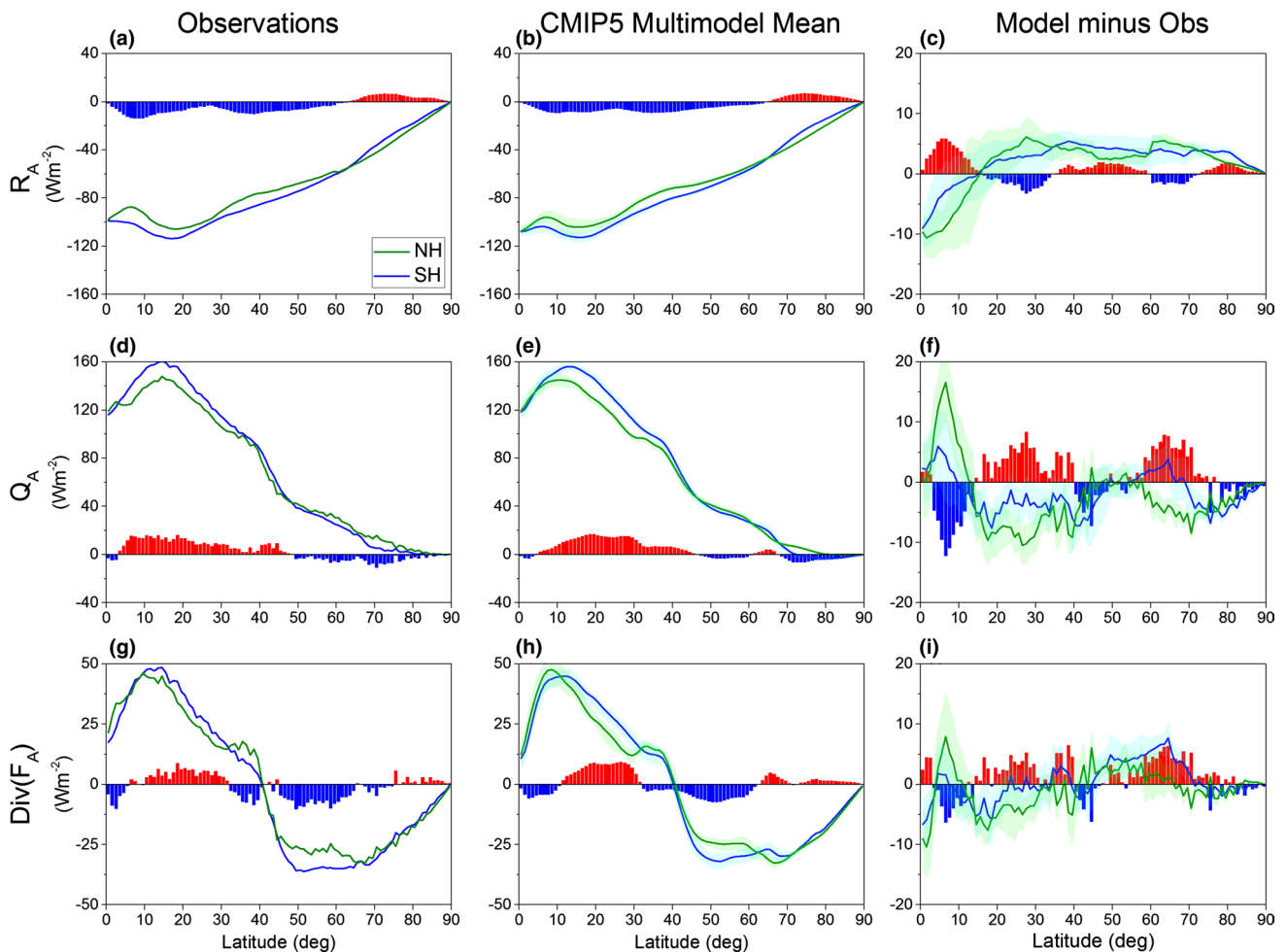
Fig. 3 Zonal mean values corresponding to regional maps in Fig. 2. *Bars* correspond to SH minus NH difference. *Shading* denotes CMIP5 model interquartile range

(Voigt et al. 2013; Stephens et al. 2015) is not replicated in the CMIP5 multi-model mean. While observations show a near-zero SW TOA contribution to HT_{EQ} (Table 2), the multi-model mean indicates 1.7 W m^{-2} more absorbed SW radiation in the SH than in the NH, corresponding to 0.22 PW SH to NH HT_{EQ} (Table 3). The longwave (LW) hemispheric asymmetry in observations and models is in better agreement, contributing approximately 0.2 PW to HT_{EQ}. As a result, HT_{EQ} from the CMIP5 multi-model mean is more than double the observed value. We note that there is significant variability amongst the individual CMIP5 models (Fig. 4a) (standard deviation of 0.33 PW). This large spread is mainly due to differences in SW TOA flux hemispheric asymmetry amongst the models (Fig. 5).

Except for LW, observed and CMIP5 multi-model mean within-atmosphere energy budget terms are consistent to 5 W m^{-2} when averaged globally and over each hemisphere (Tables 2, 3). Both the observations and CMIP5 multi-model mean results show stronger net atmospheric radiative

cooling (R_A) and combined latent and sensible heating (Q_A) in the SH compared to the NH, primarily determined by lower latitudes (Fig. 3). Consistent with the notion that AHT_{EQ} transports heat from the warmer to colder hemisphere, the hemispheric difference in R_A implies an AHT_{EQ} of 0.75 PW from the NH to the SH (Table 2). The SW component of R_A hemispheric difference contributes 0.46 PW and the LW contributes 0.29 PW. The hemispheric difference in Q_A implies an AHT_{EQ} of 0.51 PW in the opposite direction, resulting in a 0.24 PW NH to SH AHT_{EQ}. In contrast, hemispheric asymmetries in CMIP5 multi-model mean radiative and combined latent and sensible heating are nearly identical but with an opposite sign (Table 3), implying no AHT_{EQ}. However, the individual CMIP5 models show a large spread in AHT_{EQ} (Fig. 4b), with a standard deviation of 0.2 PW. In over half the CMIP5 models considered, the combined latent and sensible heat flux contribution to AHT_{EQ} dominates over the radiative contribution (Fig. 6a), implying a net SH to NH AHT_{EQ}. Of the models

Table 2 Observation based radiative and non-radiative fluxes for global, SH, and NH, and the corresponding implied cross-equatorial heat transport

	Global (W m^{-2})	SH (W m^{-2})	NH (W m^{-2})	HT$_{EQ}$ (PW)	Source
Top-of-atmosphere					
SW (Dn)	240.2	240.3	240.1	0.02	CERES, SORCE
LW (Dn)	−239.6	−238.9	−240.3	0.18	CERES
R$_T$	0.6	1.4	−0.2	0.20 ± 0.05	CERES
	Global (W m^{-2})	SH (W m^{-2})	NH (W m^{-2})	AHT$_{EQ}$ (PW)	Source
Within-atmosphere					
SW	78.0	76.2	79.8	−0.46	CERES
LW	−186.6	−187.7	−185.4	−0.29	CERES
R$_A$	−108.6	−111.5	−105.7	−0.75 ± 0.11	CERES
Q$_A$	108.6	110.6	106.6	0.51 ± 0.12	Residual
$\nabla \cdot F_A$	0.0	−1.0	0.9	−0.24 ± 0.04	ERA-Interim
	Global (W m^{-2})	SH (W m^{-2})	NH (W m^{-2})	OHT$_{EQ}$ (PW)	Source
Surface					
SW (Dn)	186.3	186.3	186.4	−0.02	CERES
SW (Up)	24.1	22.1	26.0	0.50	CERES
SW (Net)	162.2	164.1	160.3	0.48	CERES
LW (Dn)	345.1	343.4	346.8	−0.43	CERES
LW (Up)	398.1	394.6	401.6	0.89	CERES
LW (Net)	−53.0	−51.2	−54.9	0.47	CERES
R$_S$	109.2	112.9	105.5	0.95 ± 0.10	CERES
Q$_S$	−108.6	−110.6	−106.6	−0.51 ± 0.12	Residual
Fs	0.6	2.3	−1.1	0.44 ± 0.07	Residual

Period of coverage is 2001–2012

showing NH to SH AHT$_{EQ}$, only 3 models (MPI models) fall within the observational uncertainty for both Q_A and R_A contributions.

Cloud, surface and aerosol properties play an important role in determining the SW and LW contributions to hemispheric radiative heating/cooling in the atmosphere. While LW radiative cooling is greater in the NH for clear-sky conditions, the opposite is true for all-sky (Fig. 5a). The sign reversal is associated with a larger cloud fraction in the SH (Stephens et al. 2015), a greater fraction of low clouds in SH, and more high clouds in NH (Fig. 5b). These results are based upon a four-year average of merged CALIPSO, Cloudsat, CERES and MODIS (CCCM) EditionB1 data (Kato et al. 2010). Since low clouds enhance LW radiative cooling of the atmospheric column (Kato 2009), a greater fraction of low clouds in the SH enhances LW radiative cooling relative to the NH. In the SW, radiative heating in the atmosphere is greater in the NH for both clear and all-sky conditions. This is due to a higher surface albedo in the NH with its greater land fraction, which enables more light reflected from the surface to be absorbed by the atmosphere. Furthermore, since pollution is greater in

the NH, there are likely more absorbing aerosols in the NH to further increase atmospheric SW absorption. Another contributing factor is precipitable water, which is slightly greater in the NH according to ERA-Interim reanalysis.

At the surface, the CERES data suggest a global mean R_S of 109 W m^{-2}, compared to 106 W m^{-2} for the CMIP5 multi-model mean (Tables 2, 3). Since both are in near surface energy balance, values for Q_S are similar. Stephens et al. (2012) estimated an even higher value of Q_S (112 W m^{-2}). Remarkably, when Q_S is directly obtained from satellite retrievals and/or reanalysis, its value is 14–17 W m^{-2} lower than what is required to balance the radiative contributions (Stephens et al. 2012; Wild et al. 2013; Loeb et al. 2014). There is still much debate about whether our inability to close the surface energy budget in observations is due to an underestimation in precipitation/evaporation and/or an overestimation in net surface radiation (R_S) (Stephens et al. 2012; Loeb et al. 2014; Behrangi et al. 2014). However, recent studies have shown that satellite-derived downward SW and LW radiative fluxes are consistent with ground observations to within a few W m^{-2} over both land and ocean (Kato et al. 2013; Loeb et al. 2014; Rutan et al.

Table 3 CMIP5 multi-model mean radiative and non-radiative fluxes for global, SH, and NH, and the corresponding implied cross-equatorial heat transport

	Global (W m^{-2})	SH (W m^{-2})	NH (W m^{-2})	HT$_{EQ}$ (PW)	Source
Top-of-atmosphere					
SW (Dn)	239.1	239.9	238.2	0.22	Model output
LW (Dn)	−238.4	−237.6	−239.3	0.21	Model output
R$_T$	0.7	2.3	−1.0	0.43	Model output
	Global (W m^{-2})	SH (W m^{-2})	NH (W m^{-2})	AHT$_{EQ}$ (PW)	Source
Within-atmosphere					
SW	73.5	72.2	74.7	−0.33	Model output
LW	−179.0	−180.2	−177.7	−0.31	Model output
R$_A$	−105.5	−108.0	−103.0	−0.64	Model output
Q$_A$	105.2	107.8	102.6	0.67	Model output
$\nabla \cdot F_A$	−0.27	−0.16	−0.39	0.03	Residual
	Global (W m^{-2})	SH (W m^{-2})	NH (W m^{-2})	OHT$_{EQ}$ (PW)	Source
Surface					
SW (Dn)	190.3	189.8	190.7	−0.11	Model output
SW (Up)	24.7	22.1	27.2	−0.65	Model output
SW (Net)	165.6	167.8	163.5	0.55	Model output
LW (Dn)	338.3	338.6	338.1	0.07	Model output
LW (Up)	397.8	396.0	399.6	−0.46	Model output
LW (Net)	−59.5	−57.4	−61.6	0.53	Model output
R$_S$	106.1	110.3	101.9	1.07	Model output
Q$_S$	−105.2	−107.8	−102.6	−0.67	Model output
Fs	0.92	2.5	−0.66	0.40	Model output

Period of coverage is 1980–2004

Fig. 4 Cross-equatorial heat transport for **a** total (HT$_{EQ}$), **b** atmosphere (AHT$_{EQ}$) and **c** ocean (OHT$_{EQ}$) from the first 30 CMIP5 models in Table 1 and from observations (*thick line*). "Mn" corresponds to the multi-model mean value. *Gray shading* represent the observational uncertainty
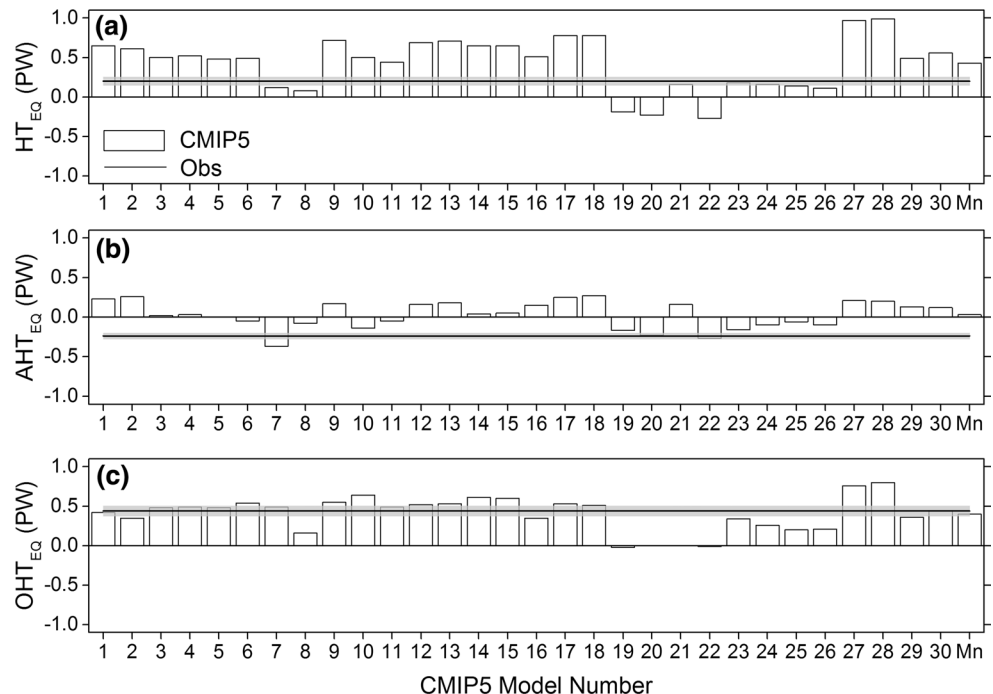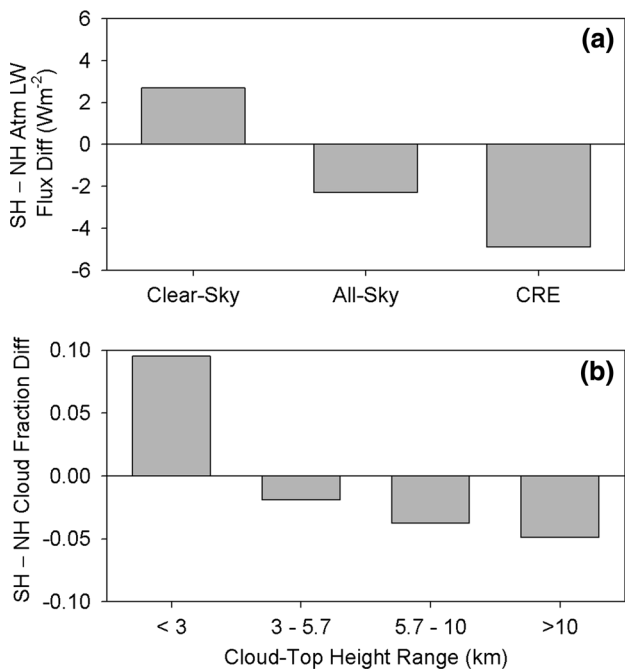
Fig. 5 a SH minus NH difference in atmospheric LW clear-sky, all-sky and cloud radiative effect (CRE). A positive (negative) SH–NH difference means more LW atmospheric cooling in the NH (SH). **b** SH minus NH difference in cloud fraction for different cloud height ranges according to CALIPSO and Cloudsat

2015). It is thus unlikely that a large positive bias in R_S is the reason for our inability to close the surface energy budget in observations.

The SH and NH hemispheric mean surface energy budgets show how the surplus of energy associated with the planetary imbalance of 0.6 W m^{-2} is distributed (Table 2). On average, the SH surface receives an extra 2.3 W m^{-2} and the NH surface loses 1.1 W m^{-2}. Assuming the hemispheric asymmetry in ocean heat storage is much smaller (e.g. Durack et al. 2014; Drijfhout et al. 2014), this implies a 0.44 PW SH to NH OHT$_{EQ}$ (Frierson et al. 2013; Marshall et al. 2013). The hemispheric asymmetry in R_S implies an OHT$_{EQ}$ of 0.95 PW from the SH to the NH and this is counteracted by the hemispheric asymmetry in Q_S, which implies an OHT$_{EQ}$ of 0.51 PW from the NH to the SH. The net downward SW and LW radiative fluxes contribute equally to the hemispheric contrast in R_S owing to a larger surface albedo and higher surface temperatures in the NH, which cool the surface more effectively. Since downwelling SW at the surface is equal in both hemispheres, the net surface SW contrast between the hemispheres is entirely due to surface albedo. With the exception of the IPSL models and MIROC4 h (models 19–22), which show zero OHT_{EQ}, all CMIP5 models show a SH to NH OHT$_{EQ}$, but only 8 models fall within observational uncertainty (Fig. 4c). In 20 of the models, SH to NH radiative and NH to SH latent

Fig. 6 Scatterplots of radiative and combined latent and sensible heat contributions to cross-equatorial heat transport for **a** atmosphere (AHT$_{EQ}$) and **b** ocean (OHT$_{EQ}$) from individual CMIP5 models, the multi-model mean, and observations. *Black solid line* corresponds to zero cross-equatorial heat transport. *Red dashed line* shows pairs of contributions that add to observed AHT$_{EQ}$ or OHT$_{EQ}$
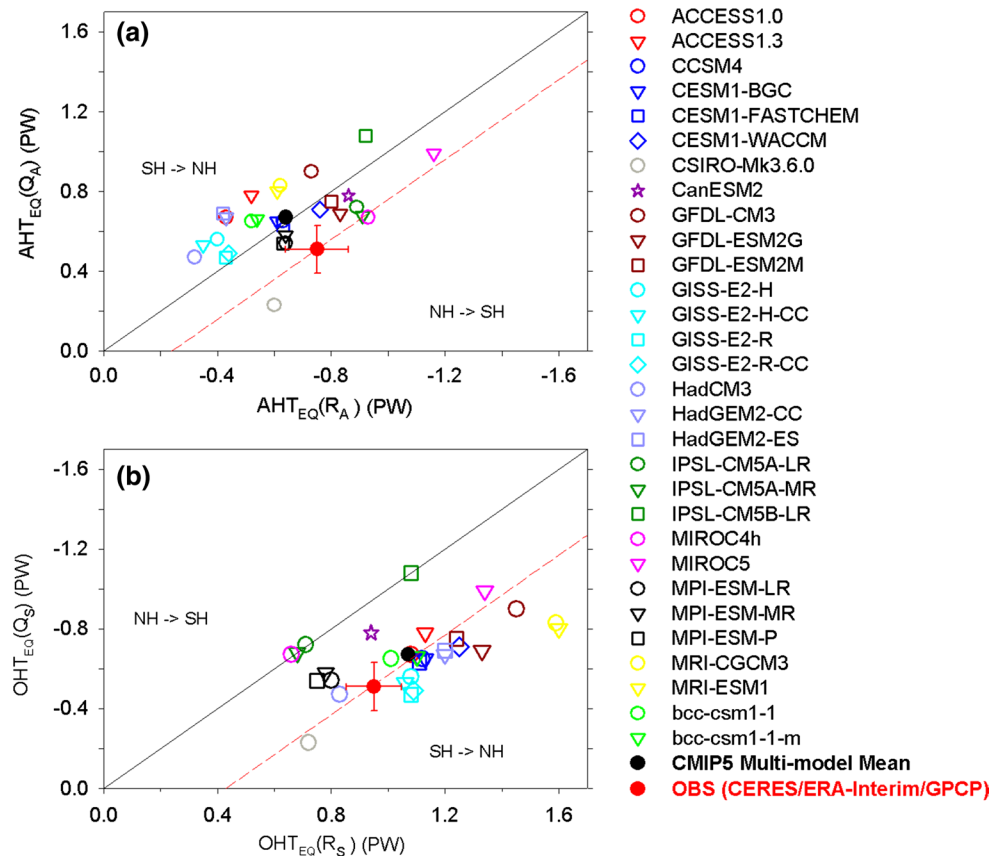
and sensible heat contributions are overestimated compared to the observations by 0.1 PW or more. Consequently, it is quite feasible for a model to have large biases in both the radiative and combined latent and sensible heat components yet still provide the correct OHT_{EQ}. This fortuitous cancelation of error masks more serious problems, some of which we explore further in the next section.

3.3 Revisiting the tropical precipitation asymmetry problem in climate models

Many studies have investigated aspects of the relationship between AHT_{EQ} and the position of the ITCZ and/or differences in tropical precipitation between the NH and SH (Yoshimori and Broccoli 2008; Frierson et al. 2013; Hwang et al. 2013; Donohoe et al. 2013; Frierson et al. 2013; Marshall et al. 2013). Contrary to observations, which show a mean ITCZ at 6°N, more precipitation in the NH than in the SH, and a southward AHT_{EQ}, climate models exhibiting a double-ITCZ and excessive SH tropical precipitation display a northward AHT_{EQ}. Idealized model experiments indicate that when perturbations in one hemisphere are imposed through thermal forcing or changes in surface albedo, the ITCZ and tropical precipitation maximum shift towards the warmer/darker hemisphere (Chiang et al. 2003; Broccoli et al. 2006; Kang et al. 2008, 2009; Voigt et al. 2014). Because the Hadley circulation in the deep tropics governs atmospheric energy transport, a displacement of the circulation towards the warmer hemisphere is required in order to transport heat away from the warmer hemisphere across the equator via the upper branch of the Hadley circulation (Yoshimori and Broccoli 2008; Frierson and Hwang 2012).

To further explore these ideas in the context of the framework used in the previous sections, we examine the hemispheric asymmetry in R_S and Q_A as a function of the tropical precipitation asymmetry index (TPA index, hereafter), defined as the NH minus SH precipitation difference divided by the tropical mean precipitation for latitudes equatorward of 20° (Hwang and Frierson 2013). The majority of models with excessive tropical precipitation in the SH (negative TPA index) overestimate net downward radiation at the surface and flux too much latent and sensible heat from the surface to the atmosphere in the SH relative to the NH (Fig. 7a, b). In addition, many of the models also underestimate the SH–NH contrast in atmospheric radiative cooling (Fig. 7c). This in turn leads to excessive heating of the atmosphere and cooling of the surface in the SH. Indeed, Hwang and Frierson (2013) find that in CMIP5 models with a negative TPA index, the tropical mean surface air temperature in the NH is similar to or less than that in the SH, whereas the opposite is true in observations and CMIP5 models with a positive TPA index. Associated with the excess heating of the SH atmosphere is a northward

AHT_{EQ} (Fig. 7d). In order to achieve the anomalous northward AHT_{EQ}, the Hadley Circulation and ITCZ are displaced southward. For the CMIP5 multi-model mean, the excessive SH–NH contrast in combined latent and sensible heating contributes 60 % to the overall bias in atmospheric cross-equatorial heat transport, while the underestimation in SH–NH contrast in atmospheric radiative cooling contributes 40 %.

3.3.1 Relationship to SW and LW surface flux biases

Both the SW and LW components contribute to hemispheric asymmetry biases in R_S in CMIP5 models that overestimate precipitation in the SH. Figure 8 shows the hemispheric asymmetry (SH minus NH) in R_S and the corresponding SW and LW contributions for models with negative and positive TPA index. CMIP5 models with negative TPA index overestimate the hemispheric asymmetry in R_S compared with CERES by 1.9 W m^{-2}, with the SW component contributing 1.2 W m^{-2} (63 %) and the LW component contributing 0.7 W m^{-2} (37 %). In contrast, the average hemispheric asymmetry in R_S for CMIP5 models with positive TPA index is within 0.1 W m^{-2} of CERES, and both the SW and LW components fall within 0.31 W m^{-2} of the corresponding CERES values.

The positive hemispheric asymmetry bias in R_S for CMIP models with negative TPA index occurs from 10° to 70° (Fig. 9b). There is a positive bias in downward SW radiation in the SH subtropics and extratropics due to an underestimation in SW reflection by clouds (Figs. 9e, 11a). Consistent with these results, Hwang and Frierson (2013) show that models with a double ITCZ have too weak a SW cloud radiative effect over the Southern Ocean due to an underestimation in cloud fraction and/or cloud optical thickness. However, results in Fig. 10e show that the cloud bias also occurs at latitudes as far north as 10°S. Regionally, a positive model bias occurs over each ocean basin in the SH, and is especially large in marine stratocumulus regions (Fig. 11a). Interestingly, CMIP5 models with positive TPA index show a negative bias in zonal mean downward SW radiation in the SH compared to CERES equatorward of 50°S (Figs. 9f, 10f), implying too much cloud reflection. This mainly occurs over the Pacific Ocean between the International Date Line and 90°W, and over the Atlantic Ocean (Fig. 11b), regions associated with trade cumulus. In the NH subtropics and midlatitudes, SW model regional biases are generally positive over land and negative over ocean, except over marine stratocumulus off the coast of North America. Thus, negative regional biases over much of the north Pacific Ocean for CMIP5 models with a positive TPA index (Fig. 11b) are largely offset by positive biases over land at the same latitudes, resulting in relatively small NH zonal mean biases (Fig. 9f).

Fig. 7 **a** R_S, **b** Q_A, and **c** R_A SH minus NH hemispheric asymmetry and **d** AHT_{EQ} against tropical precipitation asymmetry index for individual CMIP5 models and observations. *Black solid line* is a least-squares fit to the CMIP5 models
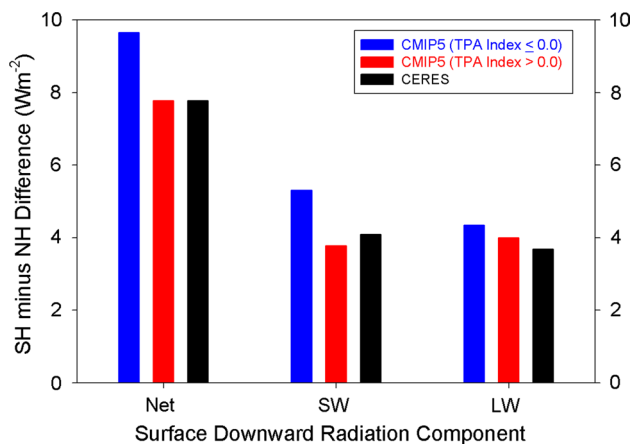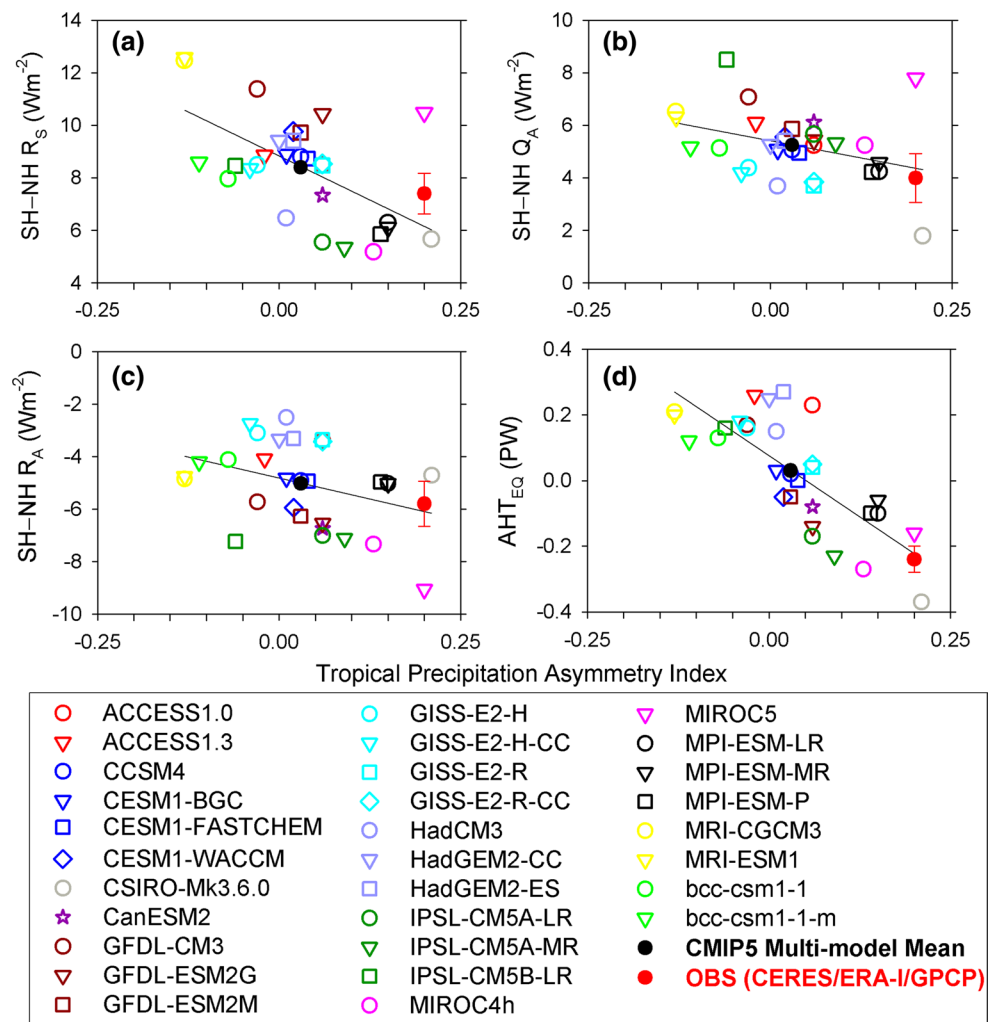

Fig. 8 SH minus NH difference in mean Net, SW and LW downward surface radiation for CMIP5 models with negative and positive TPA Index and CERES observations

Equatorward of 10° latitude, the CMIP5 models overestimate net downward SW radiation at the surface in the NH

(Fig. 9e, f), which contributes to a negative hemispheric asymmetry bias in R_S (Fig. 9b, c). Regionally, this is due to cloud biases associated with the ITCZ over the central and Eastern Pacific Ocean. Regional biases are also quite large equatorward of 10°S, but substantial cancellation of error across longitudes reduces the zonal mean bias. Poleward of 60°S, both sets of CMIP5 models overestimate net SW downward radiation (Trenberth and Fasullo 2010; Bodas-Salcedo et al. 2014).

The LW contribution to the bias in hemispheric asymmetry is mainly confined to latitudes equatorward of 30° for CMIP5 models with negative TPA index (Fig. 9h). In both hemispheres the surface LW radiative cooling is overestimated compared to CERES, but the bias is stronger for 0°–30°N, resulting in a positive bias in hemispheric asymmetry. Regionally, the model biases between 0° and 30°N are dominated by the Sahel and India (Fig. 11c) with relatively small biases over the tropical oceans where subcloud LW emission by water vapor dominates. Results for CMIP5 models with positive TPA index show a marked overall improvement, particularly over the ocean away from the equator (Fig. 11d). Biases in downward LW
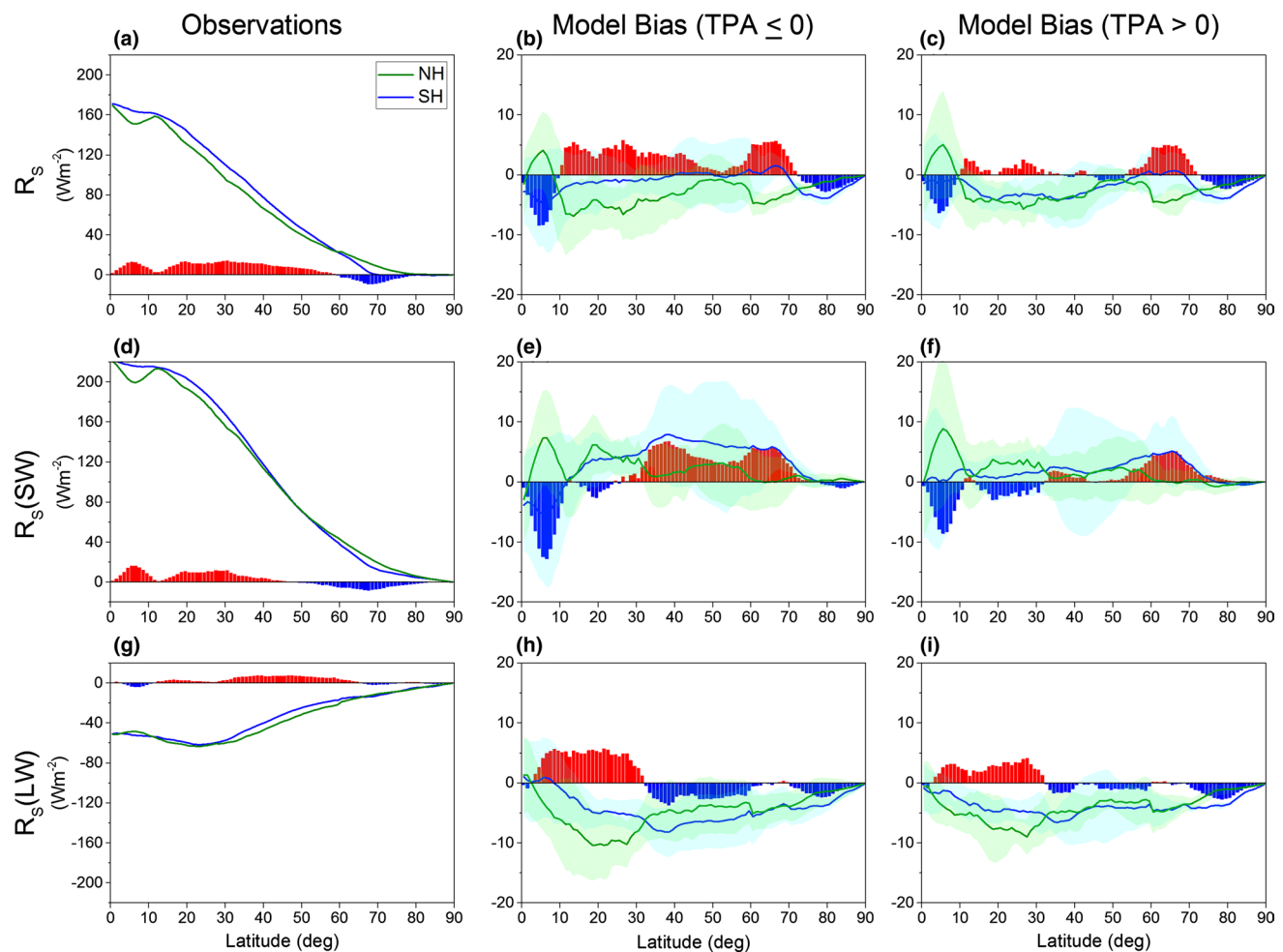
Fig. 9 All-sky SH and NH zonal mean surface radiative fluxes for **a** net, **d** SW and **g** LW from CERES observations. Corresponding CMIP5 minus observed difference for models with TPA index <0 (**b**, **e**, **h**) and TPA index >0 (**c**, **f**, **i**). *Bars* correspond to SH minus NH difference. *Shading* denotes CMIP5 model interquartile range

radiation are still negative, but their magnitude is smaller and exhibits less hemispheric asymmetry (Fig. 9i).

Thus, in CMIP5 models with negative TPA index the model bias in R_S hemispheric asymmetry is primarily due to excessive SW surface radiation poleward of 30°S (Fig. 9e) and too much LW surface radiative cooling in the NH tropics equatorward of 30°N compared to the same latitudes in the SH (Fig. 9h). In contrast, SW and LW biases in hemispheric asymmetry for CMIP5 models with positive TPA index largely cancel (Fig. 9f, i), resulting in a much smaller net bias in R_S hemispheric asymmetry (Fig. 9c).

4 Summary and conclusions

Recent studies (Frierson et al. 2013; Marshall et al. 2013) have shown strong linkages between hemispheric asymmetries in atmospheric and oceanic energy budgets,

tropical precipitation and the mean position of the ITCZ. Here, satellite-based TOA and surface radiation budget observations from CERES are combined with mass corrected vertically integrated atmospheric energy divergence from the ERA-Interim reanalysis to determine the regional distribution of the TOA, within-atmospheric and surface energy budget terms over the globe. The observed regional, zonal, hemispheric and global means are compared with simulations from 30 CMIP5 models in which the multiyear globally averaged net TOA and surface energy budgets are consistent to within 1 W m^{-2}. The atmospheric and oceanic cross-equatorial heat transports in observations and models are further decomposed in terms of radiative and combined sensible and latent heat contributions, which provides a constraint on climate model large-scale energy transport and enables new insights into the precipitation asymmetry problem in climate models exhibiting excessive SH tropical precipitation compared to observations. The results suggest
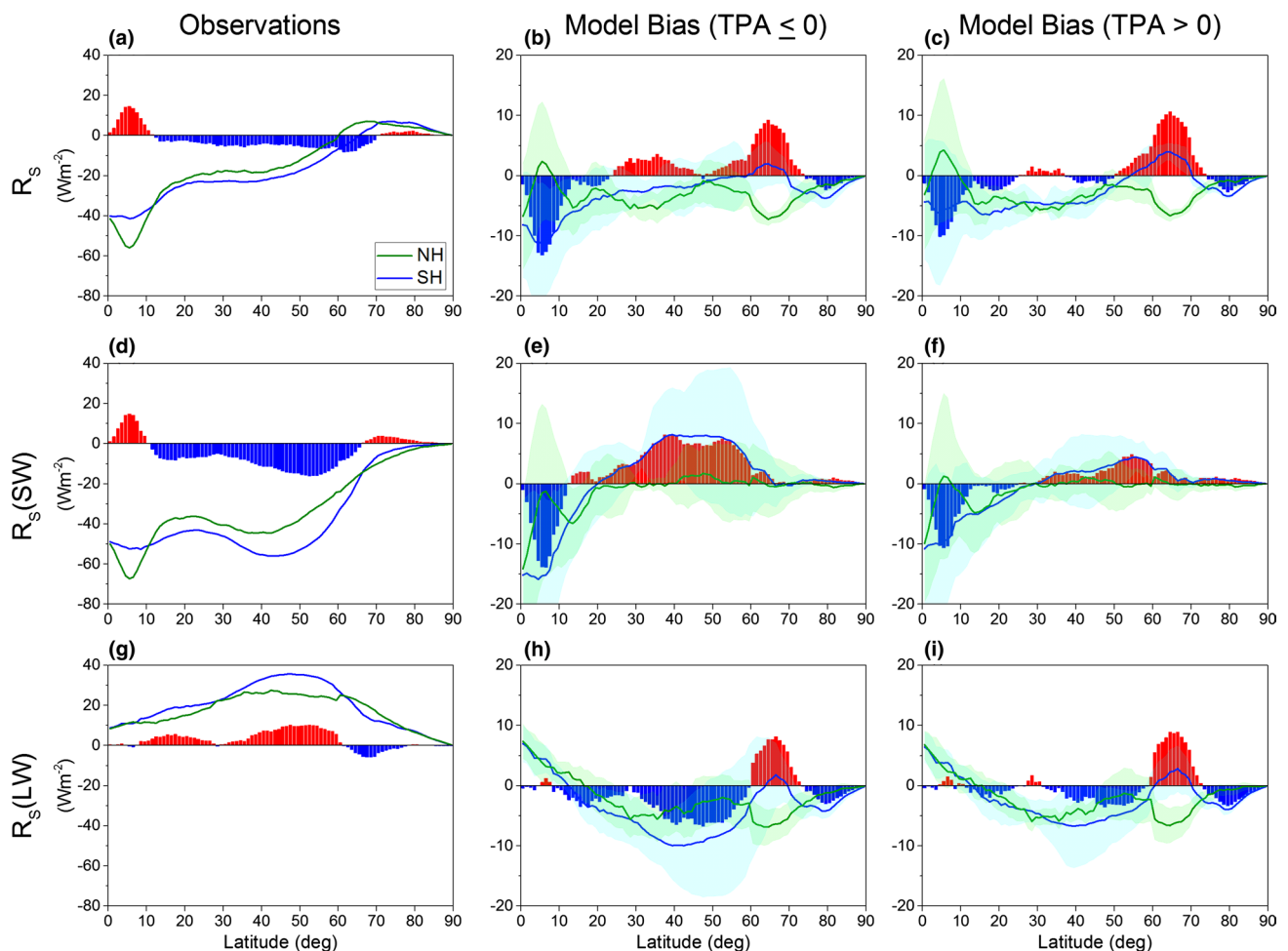
Fig. 10 Same as Fig. 9a–i but for cloud radiative effect

that the known problems in simulating tropical precipitation should not be viewed in isolation but rather as being tightly coupled to systematic biases in the energy budget, both in the atmosphere and ocean and at low and high latitudes.

While regional patterns in net atmospheric radiative flux are similar in observations and CMIP5 multi-model mean results, the models underestimate atmospheric radiative cooling off the west coasts of the Americas due to an underestimation of low cloud coverage. Atmospheric radiative cooling is overestimated in CMIP5 models in convective regions, perhaps due to an underestimation in the amount of total ice and liquid water content (Li et al. 2013). Regional patterns in surface-to-atmosphere sensible and latent heat flux are similar in observations and CMIP5 models, but there are large positive biases in the models just north of the equator over the central and eastern Pacific Ocean and negative biases in the subtropics in both hemispheres that persist even in the zonal average.

At the TOA, the observations show hemispheric symmetry in absorbed SW radiation and more outgoing LW radiation in the NH, resulting in a northward total cross-equatorial heat transport of 0.2 PW. Because CMIP5 models absorb more SW radiation in the SH than the NH, and also emit more outgoing LW radiation in the NH, the total (atmosphere and ocean) cross-equatorial heat transport in CMIP5 models is more than double that of observations. In addition, there is a large spread amongst the models due to differences in the magnitude of SW TOA flux hemispheric asymmetry.

In the atmosphere, observed radiative cooling and the sum of latent and sensible heating are greater in the SH than the NH. While combined latent and sensible heating in the NH exceeds atmospheric radiative cooling, the opposite is observed in the SH. As a result, there is a 0.24 PW transport of heat from the NH to the SH. Expressed in terms of the individual components, the hemispheric contrast in net atmospheric radiative flux implies a heat transport of −0.75 PW and the hemispheric difference in latent and sensible heat implies a 0.51
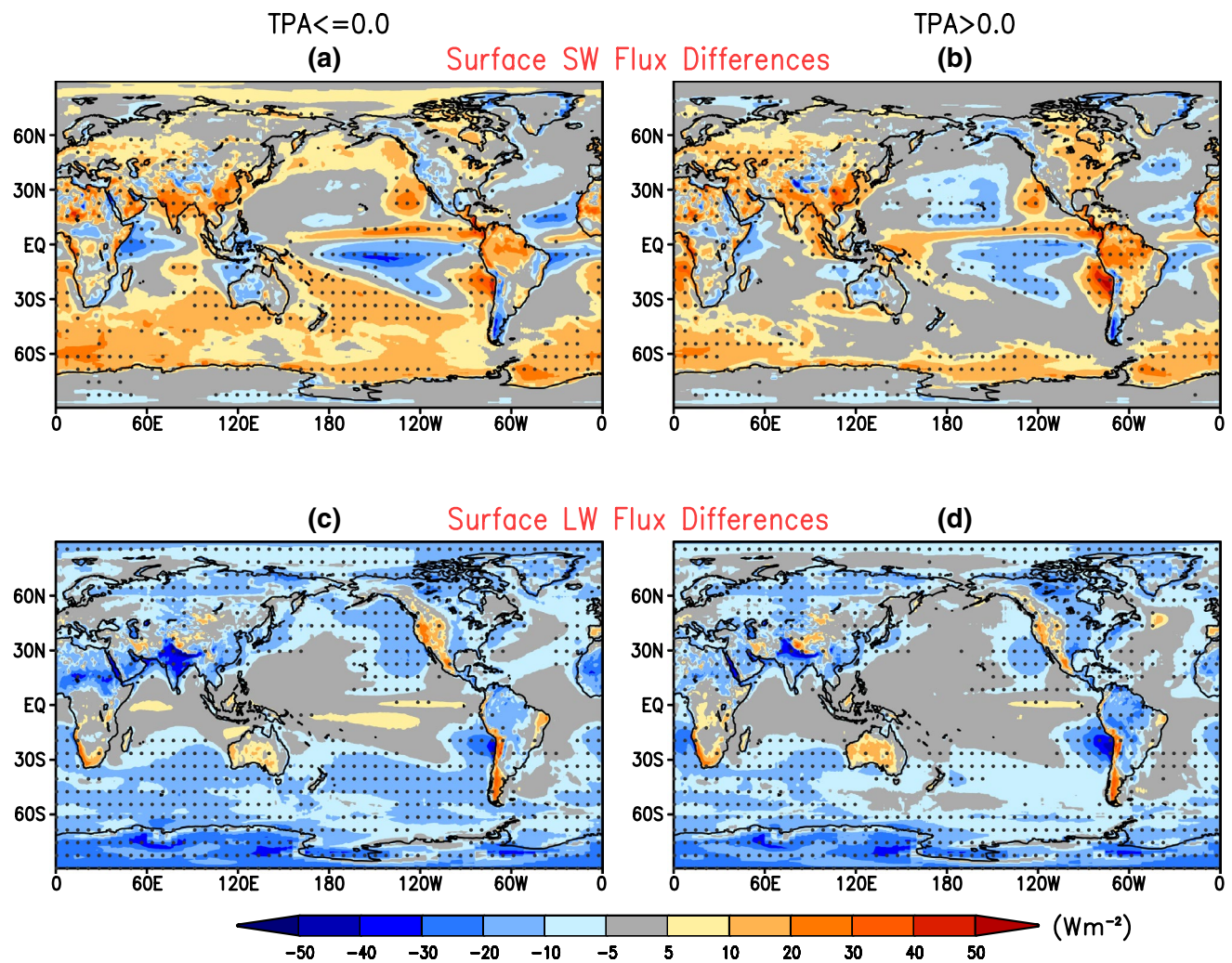
Fig. 11 All-sky CMIP5 minus CERES **a**, **b** SW and **c**, **d** LW surface flux difference for CMIP5 models with TPA index ≤0 (*left column*) and CMIP5 models with TPA index >0 (*right column*). Stippling denotes regions where the observations lie outside the model interquartile range

PW (where positive corresponds to SH to NH heat transport). The corresponding values for the CMIP5 multi-model mean are −0.64 PW and 0.67 PW, respectively, implying near zero atmospheric cross-equatorial heat transport. Only 12 of the 30 CMIP5 models considered show a NH to SH heat transport, and only 3 models (MPI models) fall within the observational uncertainty for both radiative and nonradiative components.

At the surface, the energy gain from radiation and energy loss from combined sensible and latent heating are greater in the SH than in the NH. The observed net downward radiative flux gain in the SH exceeds heat loss due to latent and sensible heat flux, while the reverse is true in the NH. The ocean compensates by transporting 0.44 PW of heat from the SH to the NH. The radiative component contributes 0.95 PW and the latent and sensible heat component contributes −0.51 PW. While virtually all of the CMIP5 models show a SH to NH OHT$_{EQ}$, two-thirds of the models overestimate the SH to NH radiative and NH to SH latent and sensible

heat contributions compared to the observations by 0.1 PW or more, suggesting that many models arrive at reasonable values of OHT$_{EQ}$ through a fortuitous cancellation of error in surface energy budget asymmetry.

Frierson et al. (2013) and Marshall et al. (2013) argue that the hemispheric asymmetry in atmospheric heating (and thus, the mean position of the ITCZ north of the equator) is a consequence of the northwards heat transport across the equator by ocean circulation. While the ocean transport is certainly important, results in this study indicate that the hemispheric asymmetry in atmospheric and surface properties also plays a critical role. Because the SH has a larger cloud fraction and a greater fraction of low clouds, while the NH has more high clouds, LW radiative cooling is more pronounced in the SH than the NH. In addition, the higher surface albedo in the NH and greater abundance of absorbing aerosols and precipitable water further contribute to SW radiative heating of the NH. The

net radiative effect is thus cooling in the SH and heating in the NH atmosphere, which enhances the hemispheric asymmetry in atmospheric heating.

The energetics framework shows that most CMIP5 models that overestimate tropical precipitation in the SH compared to observations have too much net downward surface radiation and combined latent and sensible heat flux in the SH relative to the NH. In addition, some models also underestimate atmospheric radiative cooling in the SH compared to the NH. Consequently, models that overestimate precipitation in the SH have excessive heating of the SH atmosphere and anomalous SH to NH cross-equatorial heat transport. The anomalous northward heat transport occurs via the upper branch of the northern Hadley Cell (Hwang et al. 2013). At the same time, there is anomalous transport of moisture from the NH to SH via the lower branch of the northern Hadley cell, which supplies moisture to a SH ITCZ.

For the set of CMIP5 models considered, 65 % of the hemispheric bias in net downward surface flux is from the downward SW component and the remainder is from LW. The hemispheric bias in LW surface radiative flux is due to too much LW surface radiative heat loss in the NH tropics, in particular over north Africa and India, whereas the hemispheric bias in SW surface radiative flux is associated with excessive SW surface radiation in the SH subtropics and extratropics due to an underestimation of reflection by clouds. It is plausible that the LW biases are a symptom of the unrealistic cross equatorial heat transport and resulting biases in precipitation (since drier, cloud-free conditions will enhance LW heat loss from the surface over land).

While the diagnostic framework used in this study does not solve the double ITCZ problem, it does provide useful new observational constraints on large-scale energy budget that need to be satisfied in order to make progress on this problem. This is because the large-scale circulation in the tropics and position of the ITCZ are intricately linked with the large-scale distribution of the energy budget. The decomposition can identify climate models that may provide the correct cross-equatorial heat transport, but for the wrong reason, owing to compensating errors in radiative and combined latent and sensible heat components. We caution that this approach is only really suitable for models with consistent global mean net TOA and surface energy budgets. Models that fail to satisfy this criterion have a spurious nonzero global mean total atmospheric energy divergence, which makes it difficult to meaningfully interpret model biases in large-scale transport using the energetics approached. Nevertheless, diagnostics of hemispheric asymmetry developed in the present study potentially provide a powerful constraint upon important regional biases in precipitation, of great importance in simulating current and future climate variability and change.

Appendix: Uncertainty in cross-equatorial heat transport

Total cross-equatorial heat transport (HT_{EQ})

As HT_{EQ} is determined from the hemispheric difference in R_T, any systematic bias common to both hemispheres cancels in the difference. This includes biases due to absolute calibration and conversion of measured filtered radiances to unfiltered radiances, which dominate the overall error budget in global mean flux (Loeb et al. 2009). Other error sources, such as radiance-to-flux conversion, time interpolation, and interannual variability are more random and therefore should be included.

To estimate the uncertainty associated with radiance-to-flux conversion, we compute hemispheric mean biases from SW and LW TOA flux error estimates provided in Loeb et al. (2007) (see Figs. 2, 6). Loeb et al. (2007) adapted the so-called direct integration method (Suttles et al. 1992; Loeb et al. 2003) to Terra and Aqua sun-synchronous data in order to provide regional, zonal, and global error estimates in different seasons. Zonal mean error estimates are integrated for each hemisphere and averaged over the year. This yields an uncertainty due to radiance-to-flux conversion of 0.1 and 0.2 W m^{-2} in hemispheric SW and LW differences, respectively. Assuming SW and LW uncertainties are uncorrelated, this contributes an uncertainty of 0.03 PW.

Time interpolation error arises due to incomplete sampling of the diurnal cycle and therefore can affect the hemispheres differently. To minimize temporal interpolation error, the CERES team supplements the *Terra* and *Aqua* sampling with 3-hourly (Edition 3) or hourly (Edition 4) geostationary imager measurements to estimate TOA flux changes between Terra and Aqua observations ("CERES-GEO" method). An alternate, less temporally complete method is to assume the cloud properties at the time of the CERES observation remain constant throughout the day and estimate changes in albedo with solar zenith angle and diurnal land heating using a shape for unresolved changes in the diurnal cycle ("CERES-Only"

method). Both methods are described and compared in detail in Doelling et al. (2013). The CERES-GEO method is used to create the CERES SYN1deg products and the CERES-Only method is used for CERES SSF1 deg data products. In EBAF-TOA, a hybrid method that combines aspects of both CERES-GEO and CERES-Only for SW is used, while the CERES-GEO method is used for LW (see Loeb et al. 2012, Supplementary Information for details). To compute the uncertainty in hemispheric difference due to temporal sampling, we compare hemispheric differences from EBAF-TOA Ed 2.8, SYN1deg Ed3A and SSF1deg Ed3A, and select the maximum range as representative of the uncertainty. This yields a temporal sampling uncertainty in hemispheric TOA flux difference of 0.2 W m^{-2} for both SW and LW. Assuming SW and LW uncertainties are uncorrelated, this contributes an uncertainty of 0.04 PW.

Uncertainty due to interannual variations in cross-equatorial heat transport is computed from the standard error in the 12-year mean from annual mean values of HT_{EQ}. This contributes an uncertainty of 0.016 PW. When all uncertainties are added (in quadrature), this produces a total uncertainty in HT_{EQ} of 0.053 PW or approximately 25 % of the mean.

Atmospheric (AHT_{EQ}) and oceanic (OHT_{EQ}) cross-equatorial heat transport

In this study, AHT_{EQ} is determined from the hemispheric asymmetry in $\nabla \cdot F_A$. The latter is available from NCAR (2014), which provides mass corrected vertically integrated total atmospheric energy divergence (Trenberth et al. 2011) for ERA-Interim data only (Dee et al. 2011). An alternate approach to determine atmospheric cross-equatorial heat transport is from Heaviside and Czaja (2012):

$$H_A = \int\limits_0^{2\pi R} \int\limits_{p_{100}}^{p_s} vh\frac{dp}{g}dx \tag{8}$$

where R is the Earth's radius, p_{100} is 100 hPa pressure, v is meridional velocity, R is the Earth's radius, and dx is the incremental distance along the equatorial circle $2\pi R$. A correction for mass imbalance is applied by removing from each mean v its column (1000–100 hPa) averaged value.

For the CERES period considered, when the two methods are applied to ERA-Interim, results are similar: -0.24 PW for AHT_{EQ}, and -0.21 PW for H_A. The approach in Eq. (8) is also applied to two other reanalysis products: the Modern-Era Retrospective Analysis for Research and Applications (MERRA) version 5.2.0 (Rienecker et al. 2011) and the National Centers for Environmental Prediction–Department of Energy (NCEP/DOE) Reanalysis Project (NCEP) (Kanamitsu et al. 2002). For MERRA, a value of -0.20 PW is obtained, whereas for NCEP it is -0.26

PW. Thus, the standard deviation in H_A from the 3 reanalyses is 0.032 PW, and the spread when the two methodologies are both applied to ERA-Interim is ±0.015 PW. Based upon these results, and accounting for the uncertainty due to interannual variations (0.019 PW), we estimate a 1σ uncertainty in AHT_{EQ} of 0.04 PW.

Since OHT_{EQ} is the difference between HT_{EQ} and AHT_{EQ}, we estimate the uncertainty in OHT_{EQ} to be $(0.053^2 + 0.04^2)^{1/2} = 0.066$ PW, assuming no correlation between uncertainties in HT_{EQ} and AHT_{EQ}.

Components of oceanic (OHT_{EQ} (R_S), OHT_{EQ} (Q_S)) and atmospheric ($AHT_{EQ}(R_A)$) cross-equatorial heat transport

Uncertainty in the implied cross-equatorial ocean heat transport associated with hemispheric asymmetry in R_S is estimated from hemispheric differences between surface radiative fluxes in the CERES EBAF-SFC Ed 2.8 and SYN1deg Ed3A data products. Surface radiative fluxes differ between these data products due to the different methodologies and ancillary input data sets used. Surface radiative fluxes in SYN1deg Ed3A are determined from MODIS cloud properties and GEOS 4/5 reanalysis system (Rutan et al. 2015). In EBAF-SFC, adjustments to the inputs used in SYN1deg Ed3A are made in order to ensure computed TOA fluxes are consistent with CERES EBAF-TOA. In addition to the CERES TOA constraints, EBAF-SFC uses constraints on cloud amount from CALIPSO and Cloudsat and upper tropospheric humidity from Atmosphere Infrared Sounder (AIRS) (Kato et al. 2013). The hemispheric difference in the LW and SW surface net downward flux components corresponds to 0.082 PW and 0.045 PW, respectively. When combined with the uncertainty due to interannual variability (0.029 PW), this corresponds to an uncertainty of $(0.082^2 + 0.045^2 + 0.029^2)^{1/2} = 0.098$ PW.

Uncertainty in the implied cross-equatorial ocean heat transport associated with hemispheric asymmetry in Q_S is estimated from the uncertainty in OHT_{EQ} and the contribution from the asymmetry in R_S: $(0.066^2 + 0.098^2)^{1/2} = 0.12$ PW. Finally, since R_A is given by the difference between R_T and R_S, the uncertainty in the implied cross-equatorial atmospheric heat transport associated with hemispheric asymmetry in R_A is estimated from: $(0.053^2 + 0.098^2)^{1/2} = 0.11$ PW.

References

Adler RF, Huffman GJ, Chang A, Ferraro R, Xie P, Janowiak J, Rudolf B, Schneider U, Curtis S, Bolvin D, Gruber A, Susskind J, Arkin P, Nelkin E (2003) The version 2 global precipitation climatology project (GPCP) monthly precipitation analysis (1979-present). J Hydrometeor 4:1147–1167

Behrangi A, Stephens G, Adler RF, Huffman GJ, Lambrigtsen B, Lebsock M (2014) An update on the oceanic precipitation rate and its zonal distribution in light of advanced observations from space. J Clim 27:3957–3965

Bodas-Salcedo A, Williams KD, Ringer MA, Beau I, Cole JNS, Dufresne J-L, Koshiro T, Stevens B, Wang Z, Yokohata T (2014) Origins of the solar radiation biases over the southern ocean in CFMIP2 models. J Clim 27:41–56. doi:10.1175/JCLI-D-13-00169.1

Broccoli A, Dahl K, Stouffer R (2006) Response of the ITCZ to northern hemisphere cooling. Geophys Res Lett 33:L01702. doi:10.1029/2005GL024546

Chahine MT et al (2006) AIRS: improving weather forecasting and providing new data on greenhouse gases. Bull Am Meteor Soc 87:911–926

Chiang JCH, Biasutti M, Battisti DS (2003) Sensitivity of the Atlantic intertropical convergence zone to last glacial maximum boundary conditions. Paleoceanography 18:1094. doi:10.1029/2003PA000916

Dee DP et al (2011) The ERA-interim reanalysis: configuration and performance of the data assimilation system. Q J R Meteorol Soc 137:553–597

Doelling DR, Loeb NG, Keyes DF, Nordeen ML, Morstad D, Nguyen C, Wielicki BA, Young DF, Sun M (2013) Geostationary enhanced temporal interpolation for CERES flux products. J Atmos Ocean Technol 30:1072–1090

Donohoe A, Marshall J, Ferreira D, McGee D (2013) The relationship between ITCZ location and atmospheric heat transport across the equator: from the seasonal cycle to the last glacial maximum. J Clim 26:3597–3618. doi:10.1175/JCLI-D-12-00467.1

Drijfhout SS, Blaker AT, Josey SA, Nurser AJG, Sinha B, Balmaseda MA (2014) Surface warming hiatus caused by increased heat uptake across multiple ocean basins. Geophys Res Lett 41:7868–7874. doi:10.1002/2014GL061456

Durack PJ, Gleckler PJ, Landerer FW, Taylor KE (2014) Quantifying underestimates of long-term upper-ocean warming. Nat Clim Change 4:999–1005. doi:10.1038/NCLIMATE2389

Fasullo JT, Trenberth KE (2008) The annual cycle of the energy budget. Part II: meridional structures and poleward transports. J Clim 21:2313–2325

Frierson DM, Hwang Y-T (2012) Extratropical influence on ITCZ shifts in slab ocean simulations of global warming. J Clim 25:720–733

Frierson DMW, Hwang Y-T, Fuckar NS, Seager R, Kang SM, Donohoe A, Maroon EA, Liu X, Battisti DS (2013) Contribution of ocean overturning circulation to tropical rainfall peak in the northern hemisphere. Nat Geosci. doi:10.1038/NGEO1987

Haywood JM, Jones A, Bellouin N, Stephenson D (2015) Asymmetric forcing from stratospheric aerosols impacts Sahelian rainfall. Nat Clim Change 3:660–665. doi:10.1038/nclimate1857

Heaviside C, Czaja A (2012) Deconstructing the Hadley cell heat transport. Q J R Meteorol Soc 139:2181–2189. doi:10.1002/qj.2085

Huffman GJ, Adler RF, Bolvin DT, Gu G (2009) Improving the global precipitation record: GPCP version 2.1. Geophys Res Lett 36:L17808. doi:10.1029/2009GL040000

Hwang Y-T, Frierson DMW (2013) A new look at the double ITCZ problem: connections to cloud bias over the Southern Ocean. Proc Natl Acad Sci USA 110:4935–4940

Hwang Y-T, Frierson DMW, Kang SM (2013) Anthropogenic sulfate aerosol and the southward shift of tropical precipitation in the 20th century. Geophys Res Lett 40:2845–2850

John VO, Soden BJ (2007) Temperature and humidity biases in global climate models and their impact on climate feedbacks. Geophys Res Lett. doi:10.1029/2007GL030429

Kanamitsu M, Ebisuzaki W, Woollen J, Yang S-K, Hnilo JJ, Fiorino M, Potter GL (2002) NCEP/DOE AMIP-II reanalysis (R-2). Bull Am Meteorol Soc 83:1631–1643. doi:10.1175/BAMS-83-11-1631

Kang SM, Held IM, Frierson DMW, Zhao M (2008) The response of the ITCZ to extratropical thermal forcing: idealized slab-ocean experiments with a GCM. J Clim 21:3521–3532

Kang SM, Frierson DMW, Held IM (2009) The tropical response to extratropical thermal forcing in an idealized GCM: the importance of radiative feedbacks and convective parameterization. J Atmos Sci 66:2812–2827

Kato S (2009) Interannual variability of the global radiation budget. J Clim 22:4893–4907

Kato S, Sun-Mack S, Miller WF, Rose FG, Chen Y, Minnis P, Wielicki BA (2010) Relationships among cloud occurrence frequency, overlap, and effective thickness derived from CALIPSO and CloudSat merged cloud vertical profiles. J Geophys Res 115:D00H28. doi:10.1029/2009JD012277

Kato S, Loeb NG, Rose FG, Doelling DR, Rutan DA, Caldwell TE, Yu L, Weller RA (2013) Surface irradiances consistent with CERES-derived top-of-atmosphere shortwave and longwave irradiances. J Clim 26:2719–2740. doi:10.1175/JCLI-D-12-00436.1

Li J-LF, Waliser DE, Stephens G, Lee S, L'Ecuyer T, Kato S, Loeb N, Ma H-Y (2013) Characterizing and understanding radiation budget biases in CMIP3/CMIP5 GCMs, contemporary GCM, and reanalysis. J Geophys Res 118:8166–8184

Liu C, Allan RP, Berrisford P, Hyder P, Loeb NG, Smith D, Vidale P-L (2015) Combining satellite observations and reanalysis energy transports to estimate global net surface energy fluxes 1985–2012. J Geophys Res (submitted)

Loeb NG, Loukachine K, Manalo-Smith N, Wielicki BA, Young DF (2003) Angular distribution models for top-of-atmosphere radiative flux estimation from the Clouds and the Earth's Radiant Energy System instrument on the Tropical Rainfall Measuring Mission satellite. Part II: validation. J Appl Meteor 42:1748–1769

Loeb NG, Kato S, Loukachine K, Manalo-Smith N, Doelling DR (2007) Angular distribution models for top-of-atmosphere radiative flux estimation from the Clouds and the Earth's Radiant Energy System instrument on the Terra satellite. Part II: validation. J Appl Ocean Tech 24:564–584

Loeb NG, Wielicki BA, Doelling DR, Smith GL, Keyes DF, Kato S, Manalo-Smith N, Wong T (2009) Toward optimal closure of the Earth's top-of-atmosphere radiation budget. J Clim 22:748–766

Loeb NG, Lyman JM, Johnson GC, Allan RP, Doelling DR, Wong T, Soden BJ, Stephens GL (2012) Observed changes in top-of-the-atmosphere radiation and upper-ocean heating consistent within uncertainty. Nat Geosci 5:110–113. doi:10.1038/NGEO1375

Loeb NG, Rutan DA, Kato S, Wang W (2014) Observing interannual variations in Hadley circulation atmospheric diabatic heating and circulation strength. J Clim 27:4139–4158

Marshall J, Donohoe A, Ferreira D, McGee D (2013) The ocean's role in setting the mean position of the inter-tropical convergence zone. Clim Dyn. doi:10.1007/s00382-013-1767-z

Nam C, Bony S, Dufresne J-L, Chepfer H (2012) The 'too few, too bright' tropical low-cloud problem in CMIP5 models. Geophys Res Lett. doi:10.1029/2012GL053421

National Center for Atmospheric Research (NCAR) (2014) The climate data guide: ERA-interim: derived components. https://climatedataguide.ucar.edu/climate-data/era-interim-derived-components

Rienecker MM, Coauthors (2011) MERRA: NASA's modern-era retrospective analysis for research and applications. J Clim 24:3624–3648. doi:10.1175/JCLI-D-11-00015.1

Roemmich D, Church J, Gilson J, Monselesan D, Sutton P, Wijffels S (2015) Unabated planetary warming and its ocean structure since 2006. Nat Clim Change. doi:10.1038/NCLIMATE2513

Rutan DA, Kato S, Doelling DR, Rose FG, Nguyen LT, Caldwell TE, Loeb NG (2015) CERES synoptic product: methodology and validation of surface radiant flux. J Atmos Ocean Tech (in press)

Salomonson VV, Barnes WL, Maymon PW, Montgomery HE, Ostrow H (1989) MODIS: advanced facility instrument for studies of the earth as a system. IEEE Trans Geosci Remote Sens 27:145–153. doi:10.1109/36.20292

Stephens GL et al (2008) CloudSat mission: performance and early science after the first year of operation. J Geophys Res 113:D00A18. doi:10.1029/2008JD009982

Stephens GL, Li J-L, Wild M, Clayson CA, Loeb N, Kato S, L'Ecuyer T, Stackhouse PW, Andrews T (2012) An update on Earth's energy balance in light of the latest global observations. Nat Geosci 5:691–696

Stephens GL, Brien DO', Webster PJ, Pilewski P, Kato S, Li J-L (2015) The albedo of Earth. Rev Geophys. doi:10.1002/2014RG000449

Suttles JT, Wielicki BA, Vemury S (1992) Top-of-atmosphere radiative fluxes: validation of ERBE scanner inversion algorithm using Nimbus-7 ERB data. J Appl Meteor 31:784–796

Taylor KE, Stouffer RJ, Meehl GA (2012) An overview of CMIP5 and the experiment design. Bull Am Met Soc 93(4):485–498

Trenberth KE, Caron JM (2001) Estimates of meridional atmosphere and ocean heat transports. J Clim 14:3433–3443

Trenberth KE, Fasullo JT (2008) An observational estimate of inferred ocean energy divergence. J Phys Ocean 38:984–999

Trenberth KE, Fasullo JT (2010) Simulation of present day and 21st century energy budgets of the southern oceans. J Clim 23(2):440–454

Trenberth KE, Fasullo JT, Mackaro J (2011) Atmospheric moisture transports from ocean to land and global energy flows in reanalyses. J Clim 24:4907–4924

Voigt A, Stevens B, Bader J, Mauritsen T (2013) The observed hemispheric symmetry in reflected shortwave irradiance. J Clim 26:468–477

Voigt A, Stevens B, Bader J, Mauritsen T (2014) Compensation of hemispheric albedo asymmetries by shifts of the ITCZ and tropical clouds. J Clim 27:1029–1045

Wild M, Folini D, Schar C, Loeb N, Dutton EG, König-Langlo G (2013) The global energy balance from a surface perspective. Clim Dyn 40(11–12):3107–3134. doi:10.1007/S00382-012-1569-8

Winker DM et al (2010) The CALIPSO mission: a global 3D view of aerosols and clouds. Bull Am Meteor Soc. doi:10.1175/2010BAMS3009.1

Yoshimori M, Broccoli AJ (2008) Equilibrium response of an atmosphere-mixed layer ocean model to different radiative forcing agents: global and zonal mean response. J Clim 21:4399–4423